communications earth & environment

ARTICLE

https://doi.org/10.1038/s43247-022-00491-w OPEN

Influence of conduit and topography complexity on spine extrusion at Shiveluch volcano, Kamchatka

Thomas R. Walter[1✉], Edgar U. Zorn[1], Claire E. Harnett[2], Alina V. Shevchenko[1], Alexander Belousov[3], Marina Belousova[3] & Magdalena S. Vassileva[1]

Most volcanic eruptions occur through magma pathways that resemble tube-like conduits fed from magma sources at depth. Here we combine remote sensing observations with both analog and numerical experiments to describe the extrusion of a spine at the Shiveluch lava dome, Kamchatka (Russian Far East) in April-October 2020. We show that spine growth is preceded by bulging of the dome surface, followed by extrusion in an asymmetric manner. The spine then elongates along a previously identified fracture line and bends toward the north. By repeated morphology analysis and feature tracking, we constrain a spine diameter of ~300 m, extruding at a velocity of 1.7 m/day and discharge rate of 0.3–0.7 m^3/s. Particle modeling of an extruding conduit plug highlights that the spine may have inclined to the north due to the topography and hidden architecture of the subsurface. We suggest that such complexities are rather common, where mechanical heterogeneities in the conduit material, mechanical erosion of the hidden spine buried by the co-evolving dome, as well as topographic (un-)buttressing controls directionality of spine growth and spine instability. The results presented here are relevant for understanding the growth and collapse hazards of spines and provide unique insights into the hidden magma-conduit architecture.

[1] GFZ German Research Centre for Geosciences, Telegrafenberg, 14473 Potsdam, Germany. [2] School of Earth Sciences, University College Dublin, Dublin D04, Ireland. [3] University of Tartu, Ulikooli 18, 50090 Tartu, Estonia. ✉email: twalter@gfz-potsdam.de

Lava spines are magma extrusions at volcanoes that allow rare insights into the conduit and conduit-bounding shear processes. Spines can form tall structures and gravitationally collapse, potentially generating pyroclastic density currents that affect surrounding regions. Understanding the directionality of spine growth and collapse is therefore highly relevant for hazard assessment and early warning.

Lava spines can evolve by extrusion of low-porosity and rather solid-behaving (competent) material. The extrusion is accomplished by an underlying magma-filled conduit that is geometrically constrained by enveloping shear faults[1,2]. Extrusion is commonly slow and associated with pre-eruptive outgassing and melt crystallization[3]. Lava spines evolve to spectacular features, such as the 305 m tall spine at Mount Pelée, West Indies[4], the ~40 m tall whaleback spines at Mount St. Helens (MSH), Washington, USA, in 2004–2008[5], the spines at Soufrière Hills volcano, Montserrat, UK, exceeding ~40 m in 1996[6], the ~40 m spines observed at Mount Unzen, Kyūshū, Japan in 1990–1995[7], or the ~110 m high 1968 Nautilus spine at Bezymianny, Kamchatka (Russian Far East)[8,9]. Spines that extrude to reach heights >100 m usually quickly collapse under their own weight[10], as observed for the 300 m high and 100 m wide spine at Mount Pelée in 1902. This collapse was potentially associated with pyroclastic density currents and followed by other episodes of spine growth[4,11].

Spine geometry may strongly depend on magma extrusion rates and the resulting magma rheology. Vertical spines form at low extrusion rates (below ~1 m^3/s) because these ascent rates provide more time for outgassing and crystallization. This allows the magma to solidify and strengthen, making it capable of sustaining tall vertical structures[12]. In turn, higher extrusion rates lead to more viscous rheology and blockier dome morphologies. At extrusion rates of ~3 m^3/s, massive stubby lava lobes develop[6,13]. At even higher extrusion rates of ~8 m^3/s, pancake-shaped lava lobes form before developing into explosive activity at rates >9 m^3/s[14]. Growth rates of a spine can vary considerably during an eruption episode, from cm/h to dm/h at MSH in 2004–2008[15,16]. A better understanding of the relationship between extrusion rates and conduit processes may advance the development of physics-based models. For instance, models simulating the extrusion of a solid plug modulated by rate-dependent friction at the conduit walls, may allow assessments or even predictions of the evolution and duration of eruptions[17]. Any better constraints on these parameters will also improve model simulations.

Heterogeneity in the rheology might also be expected in the area of the conduit and its shear zones, e.g., in the host rocks through which the spine protrudes. This will further contribute to the shape and directionality of a growing spine. Such heterogeneities may be expressed through microstructural and textural differences, for instance, rock permeability can span a range of seven orders of magnitude[12]. The permeability inside the spine is isotropic while at the spine margin shear zone it is highly anisotropic, showing a dominantly high vertical permeability[1]. Such heterogeneity may also play a fundamental role in volatile escape that regulates the explosivity of a volcanic system, and speculatively for shaping the extruding spines and directing their rotation and destabilization.

The role of the underlying conduit geometry on lava dome and spine morphology remains debated, for example, inclined conduits may produce inclined extrusions[18]. The development of fractures on spine extrusions are also poorly understood, and thought to be related to fluid accumulation at depth or to near-surface gravitational effects[19]. Spine extrusion is accomplished by alleged conduit-wall rock shear zones, which slip in a brittle mode, where higher porosity may facilitate shearing at low pressures and greater depths[3]. Previous studies highlight that shearing at shallow depths mainly occurs in a brittle way[20], such that the growth of spines is associated with characteristic drumbeat seismicity and conduit-margin fault gouges[1,2,5–7,18,21,22]. Observations of these features are challenging and remain rare, as geophysical instruments must be placed very close to a spine, and remote sensing techniques require very high resolution.

At MSH, rare detailed observations of discrete and stacked seismic events indicated slip (~5 mm) along small faults at the conduit margins[2,5,18]. Close analysis of time-lapse camera data at MSH suggests that spine growth was repeatedly interrupted by short–term meter-scale downward displacements, indicative of a gravity-driven response[19]. Spines at MSH that could be studied in detail expressed a 1–3 m thick mantle of faulted rock with striated fault gouge, cataclasites, and angular breccia[15,22,23]. This is indicative of pronounced strain localization at the conduit walls, leading to the conclusion that spines (and whaleback structures) develop if material strength is high due to a magma that has lost its porosity[12,24]. Details on the timing of the strain localization and resultant decoupling of the spine from the dome have not yet been measured geodetically, however. The fault gouge is variably densified, which at slow magma ascent rates (such as during spine extrusion) is capable of producing stronger and less permeable cataclasites[25]. Extrusion, therefore, at MSH and elsewhere, involves brittle and ductile conduit materials depending on rock porosity and crystallinity, where ductile behavior becomes more relevant at slow extrusion rates and brittle behavior dominates at fast extrusion rates[12].

These complexities during the growth and destabilization of spines must be well understood in order to better assess associated hazards. There is therefore an urgent need to find ways to safely monitor and better understand spine growth. In this work, we report on the extrusion of a spine at Shiveluch volcano, Kamchatka, Russian Far East, a volcano of dominantly andesitic composition[26]. The volcano is located to the north of the Klyuchevskaya volcano group and is affected by a regional SW-NE tectonic trend[27]. Shiveluch volcano is thought to have formed more than 80 ka before present (BP)[28], and had at least 8 sector collapses, starting from 10 ka BP[29]. Shiveluch was active, then quiet for 15 years until a sector collapse occurred in 1964, followed again by a 16-year period of quiescence and degassing before activity resumed[30,31]. The 1964 sector collapse produced debris-avalanche deposits with a volume of 1.2 km^3, that together with deposits of the associated Plinian eruption (0.8 km^3) cover the volcano's southern flank[31] (Fig. 1). This eruption was one of the largest historical explosive eruptions of Kamchatka and left a deep amphitheater open to the SW. The amphitheater opening direction aligns with a debated SW-NE tectonic trend, traceable by an alignment of monogenic cones[32], and by fractures and vents aligned high up at the summit[33]. The structural feature identified at the summit was interpreted as a fracture zone striking SW-NE and controlled repeated moderate-size collapses of a growing dome[33]. The subsequent eruptive activity changed to a spectacular episode of spine growth as described below.

Results

Field observations and webcam imagery. Field photographs taken from a distance of 9 km with a DSLR camera and telephoto lens on the same day (September 28, 2020) reveal a rounded extrusion shape reminiscent of a whaleback when viewed from the SW, with striations aligned with the spine's long axis (Fig. 1b). Side views (see also Supplementary Fig. 1) show that the northern portion of the spine developed tension fractures, open near a collapsing cliff surrounded by broad rocky talus (Fig. 1b). The first reports of changes were based on simple webcams (Fig. 2),

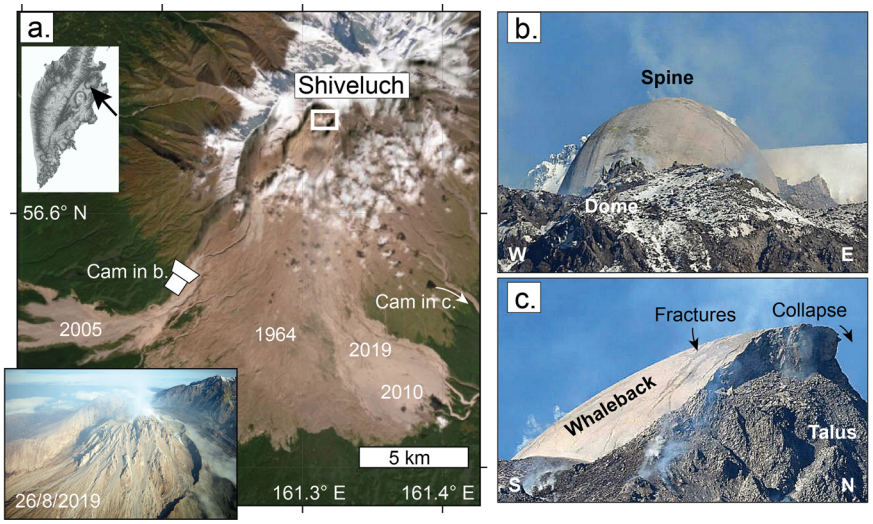

Fig. 1 Spine growth at the Shiveluch volcano. a Satellite and helicopter image illustrating the scale of the Shiveluch volcano, its horseshoe-shaped amphitheater, the 1964 debris avalanche, and the 2005, 2010 and 2019 pyroclastic density current deposits on the southern flank (years of deposition shown in figure). **b**, **c** Photos from the south (top) and from the southeast (bottom) showing the whaleback spine on September 28, 2020 (photos by Yury Demyanchuk, see **a** for camera (Cam) location). Note the sharp cliff and fractures on the northern side, as well as striations on the whaleback. The map in **a** was created using ArcMap vs. 10.8.1.

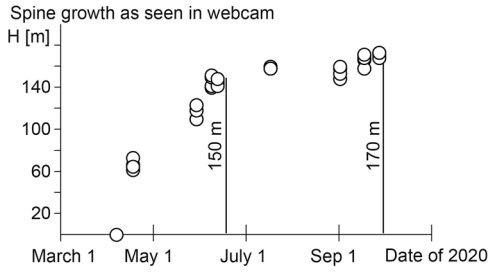

Fig. 2 Spine growth tracking derived from webcam data at 43 km distance. Tracking results suggest a spine height growing quickly between March and June 2020, reaching 150 m in June (i.e., the first three months), and then only slowly increasing to 170 m over the following three months.

which is a key observation tool for volcanoes in remote and inaccessible areas. Analysis of webcam images located ~43 km to the SSW of the volcano's summit (Supplementary Fig. 2) revealed the growth of a lava dome and then a spine on April 6, 2020, which rapidly grew in height to over 100 m within 2 months by 9 June (Fig. 2). Maximum height tracking quantified an initially sharp vertical growth, which gradually slowed down after 18 June, accumulating a total height of 170 m by September 28, 2020.

Radar and photogrammetry observations. We closely monitored the Shiveluch spine extrusion by satellite radar and photogrammetry. Radar waves backscattered to the TerraSAR-X satellite allow monitoring of the dome and spine evolution at approx. 1 m pixel (px) resolution (Fig. 3). As the radar provides its own illumination, the sensor operates independent of sunlight and even penetrates ash and steam clouds, therefore providing a temporal resolution not approached by any other methods (Supplementary Fig. 3). The radar reflections confirm the emergence of a spine on April 24, 2020 (Fig. 3c), which then gradually gained in dimension and extended toward the north. Analysis of the pixel offset helps to identify the deformation field associated with spine formation. We identify a deformation area affecting a large part of the volcanic cone two months prior to spine extrusion, with 6–8 px (about 6–8 m) displacement within an 11-day repeat pass (Fig. 3a, b). Associated with the first emergence of the spine on April 24, 2020, the displacement area sharply decreased (see also Supplementary Fig. 4). Widespread deformation of the dome is virtually absent during spine extrusion, indicative of a mechanical decoupling of the spine and the dome.

Helicopter aerial and *Pleiades* satellite stereo-photogrammetric data were acquired before and during spine growth. They provided decimeter-scale resolution, and allowed us to generate georeferenced orthophotos and digital terrain models (DTMs) that showed morphological details during three episodes of growth. Before spine growth, on October 22, 2019, the surface of the lava dome hosted small craters enclosing a 500 m wide depression (Fig. 4a). These craters together with a steep collapse scar to the eastern side developed ~1 year prior to the spine growth[33]. During spine growth, the first clear sky tri-stereo satellite image was acquired on October 01, 2020, revealing an SW-NE elongated extrusion body, 2684 m ASL, ~150 m wide and ~300 m long, with a 110 to 150 m wide talus at 2570 m ASL (Fig. 4b). The polished flat surface of the spine is well visible in satellite data, which is up to ~230 m long and 150 m wide in the Pleiades imagery. This agrees with estimates we also derived from Planet Labs satellite images, showing an increase of the polished spine surface long-axis, with 154 m on August 6, 2020, 171 m on August 16, 174 m on September 4, and 248 m on October 13, 2020 (Supplementary Fig. 5). Three-dimensional point cloud reconstruction (Supplementary Fig. 6) shows that the elongated spine is 114 m above the talus and 220 m above the previous 2019 crater, and at its highest point even 300 m above the 29 Aug 2019 collapse scar (Fig. 5). Another satellite dataset acquired 12 days later visually reveals only minor changes, but is particularly useful for analyzing late-stage spine extrusion rates.

The Pleiades tri-stereo satellite images used to generate topography data (see Fig. 4b, c) were also used to study small scale displacement and fracture formation during spine extrusion (Fig. 6). Both images highlight the presence of along-axis striations and mainly across-axis open fractures (seen by dark and shadowed cracks). The striations are aligned with the spine's long axis. Closer inspection of the striations reveals that they

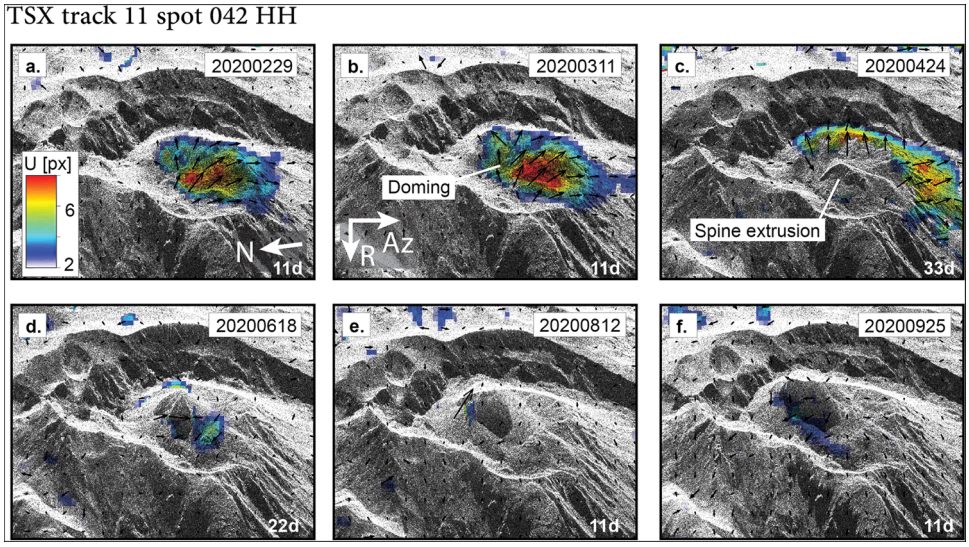

Fig. 3 Radar amplitude observations. Color represents pixel offsets calculated at cross correlation windows of 32 × 32 pixels minimum, for data pairs of single, double or triple repeat pass (with 11 day, 22 d, and 33 d time window). Displacement U is shown in pixels [px]. **a** Up to 7 px displacement affects the summit region. **b** Displacement increases to 8 px in 11 days (**d**). **c** With first spine extrusion, the large displacements disappear. **d** Minor displacement of the dome, while the spine extrudes. **e** Spine extrusion continues, migration northwards. **f** The spine widens and/or bends further to the NE. Note the occurrence of doming first, then spine extrusion (without doming). Images shown in radar coordinates (azimuth in *x*-axis, range in *y*-axis), 1 px is 1 m² approximately, descending TSX track 11 spot 042 HH. North to the left, east is up, west is down.

strongly resemble slickensides, with smooth rock surfaces and parallel grooves and scratches. The striation alignment is evident both in orthophotos and in topography, with ridges up to 2 m high, regularly spaced at 4–5 m at the spine apex, and larger 8–14 m spacing at the spine flanks (Supplementary Fig. 7). Similar to striations found elsewhere (Supplementary Figs. 8, 9), their documented presence at the Shiveluch spine characterizes pronounced shear localization and a kinematic decoupling from the dome. In this 12-day period, we further find an offset of fractures that evolved orthogonal to the striations. Existing fractures enlarged, and new fractures developed in the October 13, 2020, image (Fig. 6a, b). Pixel offset calculations suggest a mean displacement for the spine of 20.4 m in the 12 days (see inset in Fig. 6b), or a mean of ~1.7 m daily. Assuming this represents the extrusion rate and the satellite nadir-view represents the conduit outline (diameters circular 150 × 150 m², elliptical 150 × 300 m²), the extrusion volume was 0.3–0.7 m³/s, which is comparable to the rates observed at spines elsewhere[6,13,14].

Our deformation analysis suggests a mechanical decoupling of the spine from the dome, with high displacements of the spine and very low displacements of the dome (Fig. 3). The presence of striations may suggest a high strain rate, and a polished spine surface may indicate fault gauge formation. Our lineament analysis also reveals striations located on the lower (southwestern) proportion of the whaleback. These are constant in both datasets with a striation azimuth of N040°−060° (Fig. 6c, d) for weighted polylines of 5651 and 5816 m cumulative fracture lengths for the October 01 and October 13 images, respectively. The analysis of the fractures dissecting across the spine reveals azimuths N120°−155° estimated for 7188 and 5816 m cumulative fracture lengths for the October 01 and October 13 images, respectively. Most fractures are located near the steep cliff in the NE on October 01, 2020, and are bimodally distributed near the lower plateau and also near the steep cliff on October 13, 2020 (Fig. 6e, f). The upper fracture region may be associated with rock falls and unloading of the frontal steep slope of the spine. The lower region of fractures is more evident in later images, and may be associated with bending or tilting of the spine as a whole. Therefore, the two satellite images reveal the occurrence of both fractures and striations, as well as the presence of a cliff and collapse of the current spine above an underlying collapse scar.

Modeling directed conduit extrusion. To study the dynamics and asymmetry of spine growth and NE-directed collapses and to understand the mechanical decoupling of the spine and the dome, we designed both numerical and sandbox models (Fig. 7a, b). The numerical models were designed in 2D and well constrained, while the sandbox models were in 3D and were less well constrained but allow natural variations in the used materials. Both model setups were complimentary so that an initial doming episode is followed by a spine-extrusion episode. A necessity for the transition from normal dome growth to spine extrusion is the extrusion of a highly competent and cohesive material[24]. We tested a large set of geometric and dynamic models, with end members ranging from homogeneous conduit material with horizontal topography, up to heterogeneous conduit material and topography-affected models (see Supplementary Figs. 10, 11). Generally, the models begin with extrusion of a blocky material and endogenous growth of the dome, with marginal slopes depending on the angle of repose and a mound-shaped dome top. Then the spine protrudes on top of a mound-shaped dome. Talus slopes continue to approach the same internal friction angle so that additional slumps on the margins are observed, while the central spine remains symmetrical and vertical. Once shear fractures delimiting the spine evolve, the dome deforms at a reduced rate. The difference in surface textures between the spine and the dome could result from material heterogeneity, but could also relate to changes in magma-conduit wall dynamics when more competent rock is extruded.

We find that spine extrusion can become asymmetric, or directed, if we consider stiffer material on one side, and weaker material on the other side of the conduit (Fig. 7a, b). Although this situation is hypothetical, we note that the extrusion models that consider both topographic complexity and a heterogeneous conduit material, are able to well reproduce directionality and

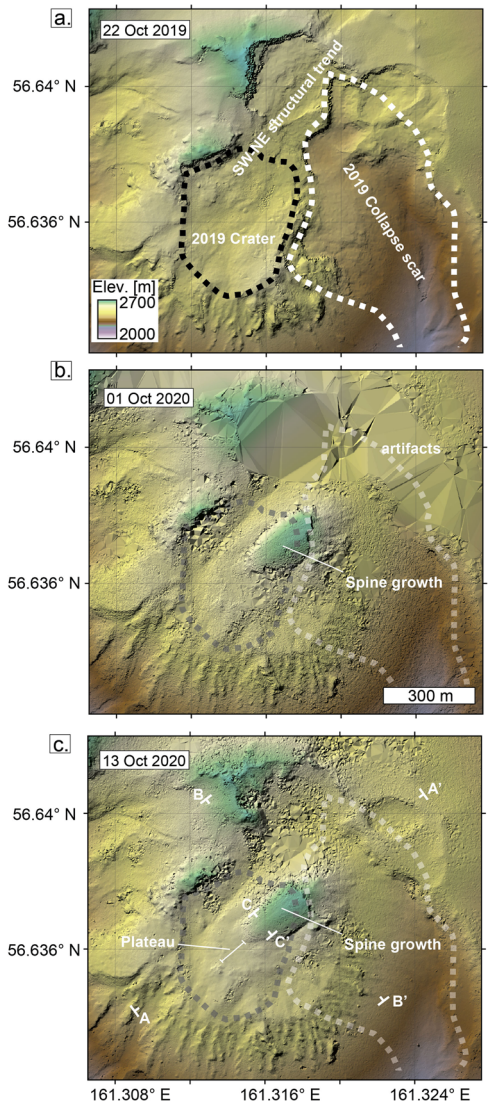

Fig. 4 Digital terrain models (DTM) produced from stereo imagery. a A DTM on October 22, 2019 (before the spine growth) reveals the presence of a number of summit craters roughly aligned along the SW-NE structural trend defined in ref. [33]. Note the deep collapse scar that formed in 2019 on the eastern part of the edifice. **b** DTM on October 01, 2020, shows the presence of a spine, partly overflowing the 2019 collapse scar. **c** DTM on October 13, 2020, shows continuous spine growth, yet cloud artifacts in the northeast. Section locations shown in **c**. Map created using ArcMap vs. 10.8.1.

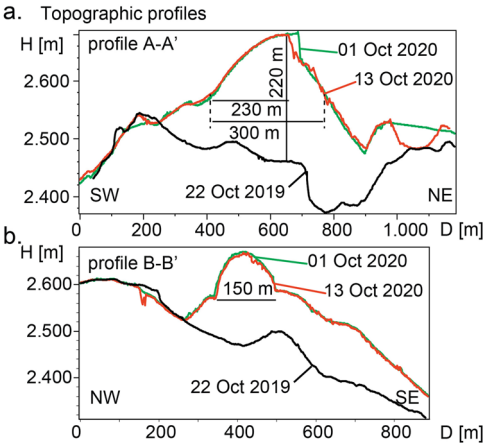

Fig. 5 Temporal evolution and dimension. Topographic profiles through the DTM data in **a**. SW-NE direction (profile A-A') and **b** in NW-SE direction (profile B-B') reveal the spine height is 220 m above the pre-existing topography, where a large amount of the elevation change is due to dome formation and talus materials. Note that the vertical cliff of the spine co-locates with the buried cliff of the 2019 collapse scar. Data highlights major topographic complexity prior to dome and spine growth, but also contains local data artifacts, e.g., at the NE part of profile A-A'.

growth of a whaleback-like spine. To simulate spine growth over a collapse scar (such as the 2019 scar at Shiveluch, Fig. 7a) we consider topographic effects and repeat the models. We now find an asymmetric talus, with the plateau on the buttressed side being higher than the unbuttressed side (Fig. 7). We also see a preferred lateral growth in the upper dome regions towards the unbuttressed side (Fig. 7c, d). Closer analysis of shear localization reveals that the spine is delimited by well-defined shear faults and initially extrudes vertically. In models, shear localization is most apparent on the buttressed side of the conduit, where striations and clear whaleback planes can be expected. With continued spine extrusion, the shear faults located closer to the buttress lead to mechanical decoupling of the spine, and the general extrusion becomes asymmetrical (Fig. 7e, f) with the spine increasingly inclined as lateral displacement dominates over vertical displacement.

Consequently, although the models are simplified, they highlight the importance of pre-existing topography and/or heterogeneous conduit material in controlling whaleback-like spine extrusion and the evolving internal deformation of a dome. We note that the relative scale of the modeled spine is smaller than that of Shiveluch. At a critical height, the spine partially collapses on one side (this can be both the buttressed or unbuttressed side), resulting in a detached and laterally inclined spine surface. It also shows a large portion of the spine to still be hidden in the shallow subsurface. With the emergence of the dominant shear faults, the internal dome deformation is rather small, which is in agreement with decoupling observations made at Shiveluch volcano.

The overall topographic expression of the models (Fig. 7) well matches the observed deformation (Fig. 3) and topographic profiles (Fig. 5), where the vertical cliff on the unbuttressed side co-locates with the buried collapse scar from 2019.

Discussion and conclusion

This study highlights that spine extrusions can provide a unique insight into hidden magma pathways and conduit geometry. The lifetime of a spine is short, because the structures are inherently unstable and often destroyed by gravitational collapse and/or volcanic explosions. Consequently, only a few spines worldwide have been investigated in greater detail, but the new Shiveluch activity provides a rare opportunity to study mechanisms controlling the extrusion and morphology of the spine. We studied the first episode of spine growth in 2020, which has collapsed by the end of 2020 and restarted again in early 2021. The Shiveluch lava dome and 2020 spine growth show a directionality towards a pre-existing depression that formed during the 2019 eruption and partial collapse, leaving a sharp and deep ravine. Previous work hypothesized that non-vertical spine extrusion occurs due to inclined conduits at depth beneath the MSH spine[18] or variably inclined conduits beneath the Soufrière Hills spine[6]. Our study also suggests that inclined spines are affected by topography.

Such directionality of spine growth and associated collapse was also observed during spine extrusion at Mount Pelée[34]. A reassessment of the old records and topographic assessments at

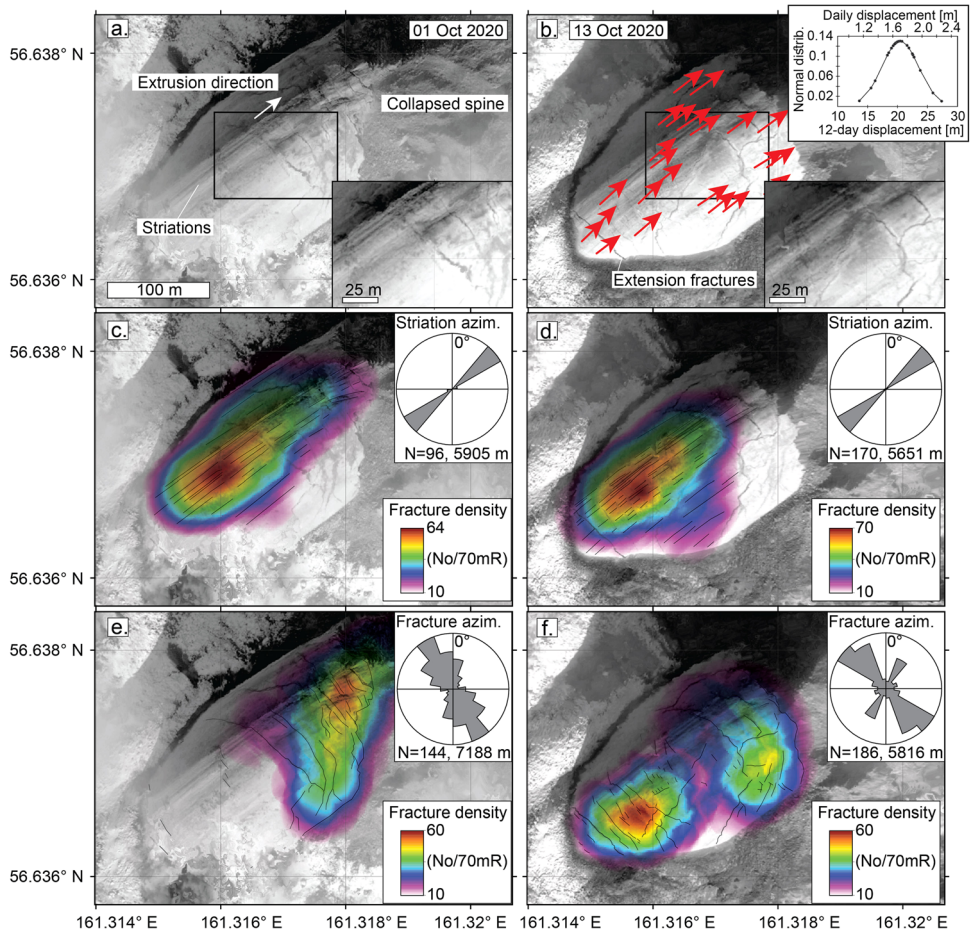

Fig. 6 Displacement and fracture analysis. The 2020 Shiveluch whaleback spine, shown for two satellite image datasets (October 1 and 13, 2020). **a** Striations have developed in a NE-SE direction, sub-parallel to the N54°E azimuthal elongation direction of the spine. Fractures show opening perpendicular to the elongation axis. **b** The following satellite data (12 days later) reveals similar striations, but fractures have been displaced to the NE by a cumulative mean of 20.4 m, as determined by pixel tracking. **c**, **d** Striation density analysis reveals clustering at the lower SE flank of the whaleback, with orientation NE-SW shown by the 48 polyline features weighted by length to 2940 elements, the mean directions at 56° in rose plot, and an angular deviation of only 5.1°. **e**, **f** Fracture density concentrates near the spine collapse region at higher elevations (above 2660 m). Statistics and rose plots show the 72 features weighted by length to 1649 elements, the mean directions at 132° with an angular deviation of 59.6°. Pleiades TriStereo data was analyzed in ArcMap vs. 10.8.1., rose diagrams generated using Polar Plots and Circular Statistics[60].

Mount Pelée[4] indicate a strong asymmetry of the growing dome and collapse direction, with steeper slopes (40–50°) to the NE and shallow slopes (15°) to the south, thus a similar topographic control may have played a role. The southern direction was open and lavas gradually flowed or crumbled into a pre-existing deep valley of the Rivière Blanche[4]. Our analysis reveals spine collapse at a location where underlying topographic kinks in slope were present. Therefore, detailed knowledge of the previous topography is essential to understand the direction of collapses and pyroclastic hazards at Shiveluch, and to understand past events of directed spine growth elsewhere. Additionally, our modeling reveals that such a topographic configuration is directing broad internal shearing and lateral motion of materials towards the unbuttressed side.

Our kinematic modeling considering topographic and material effects convincingly explains the deformation, location of striations, and directed growth and collapse of the spine. Data on the morphology and extrusion rate of an active spine on a growing lava dome can be interpreted in terms of the parameters characterizing the shallow magma system which feeds the dome and spine. However, such interpretation strongly depends on the selection of the conceptual model of the magma-feeding system of the dome and spine. Currently, there are two principally different conceptual models of the magma systems feeding dome-forming eruptions: (1) a classic vertical or inclined cylindrical conduit, which is continuously filled with ascending magma[35], and (2) a feeding system composed of several elongated magma batches that rise one-by-one[36]. If we hypothesize that the second model is valid and serves to explain the episodic dome growth at Shiveluch, an open question remains regarding the length and volume of the ascending elongated magma batches. Based on our measurements, we estimate that the length of the extruding and solid spine accumulates to as much as half a kilometer in length (excluding the dome material that erupted before). Furthermore, a considerable magma volume was added during the dome forming eruption, which may provide a first-order idea that the elongated magma batches are on the kilometer scale. Shortly after the observations reported here, a pronounced extrusion pause occurred, followed in 2021 by another extrusion event of similar duration and scale.

We used a combination of field cameras, satellite radar backscattering amplitude images, and stereo photogrammetry to characterize the evolution of an extruding spine and quantify its growth, fracturing, and instability which are mostly reproduced by both analog and numerical models. The ascent rate of magma in the conduit (or, accordingly, the ascent rate of the uppermost

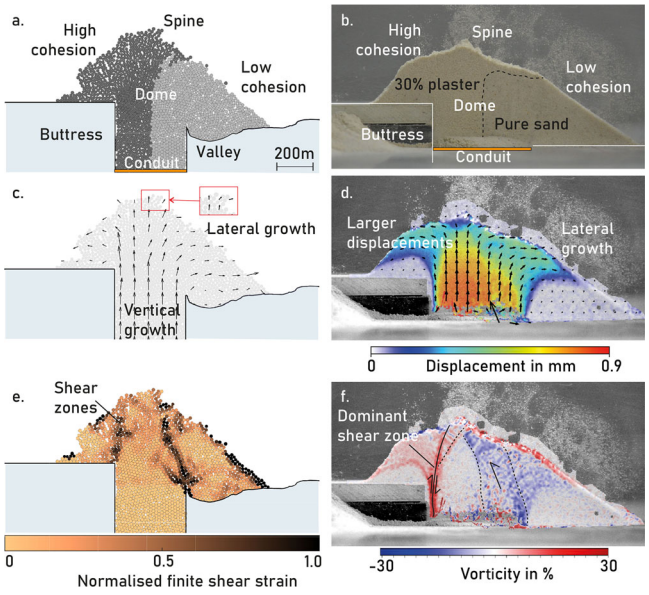

Fig. 7 Computational particle flow and analog modeling. a 2D PFC model and **b** analog sandbox model, both showing high and low cohesion material extruded from a conduit, with a stable buttress to the left side of the conduit exit. **c**, **d** Velocity vectors showing primarily upward movement above the conduit, with lateral flank motion. Spine emplacement can be seen at the top of the dome, where the cohesion contrast is forcing direct lateral motion. **e**, **f** Strain accumulation showing fault formation broadly in line with the conduit exit. Data in **f** is displayed as vorticity, which represents shear strain.

magma batch) is about 1.7 m/day. Hence, the average discharge rate (0.3–0.7 m^3/s) of magma during the period of observation was up to 6×10^4 m^3/day. The upper part of the conduit is filled with highly viscous magma that probably still contains some melt phase that allows the spine to deform plastically under its own weight to obtain the *whaleback* or *nautilus* appearance.

The great spine at Mount Pelée that extruded through the dome from 3 to 4 November 1902, assuming it had not suffered collapses, would have accumulated to a cylinder that measures 850 m in height and 150 m in diameter[34]. The 2020 spine at Shiveluch grew 135 m within the first 3 months (Fig. 2), which translates to a daily vertical growth of 1.5 m. Later analysis in October suggested a mean displacement of 20.4 m within 12 days, translating to a daily displacement of 1.7 m. Assuming these numbers represent a constant growth rate since March 2020 and assuming no material is lost by collapse and bending, the spine could have reached 315–590 m in height by October 2020. This highlights that there is (i) a significant loss of material by collapses and (ii) the depth extent of the uprising magma plug is up to half a kilometer depth. A similar rapid initial vertical growth, followed by a decaying vertical growth rate (as shown in Fig. 2), has been observed during previous dome and spine emplacement episodes at other volcanoes (e.g., St. Vincent[37]; Volcán de Colima[38]; Soufrière Hills Volcano[39]), as well as being well replicated by previous particle-based numerical models (similar to those used here) that use a cohesive material[38].

We have inferred that the upper part of the conduit of Shiveluch has a circular, or maybe oval, cross-section with a diameter of about 200 m. This may be a simplification, as satellite imagery suggests the whaleback is elongated SW-NE, which is also the same alignment of a structural trend described earlier[33]. For instance, located only 400 m to the NE of the spine is an explosion crater, aligned with the structural trend. The TerraSAR-X data reveals a gradual shift of the spine width and location towards the NE, which could be indicative of a rather elliptic conduit.

The Shiveluch spine has some striking geometric and structural similarities to some of the seven spines that were sequentially extruded during the 2004–2008 eruption at MSH[15,40]. All of these spines were bounded by a 1–3 m thick gouge zone[15] and extrusion was accompanied by *drumbeat* seismicity[2] and small sporadic volcano-tectonic earthquakes[41]. At Shiveluch, seismic networks were likely too far away or not sensitive enough to record seismicity. Our modeling shows extrusion of spines through a dome if the material is stiffer or mechanically more competent (cf. ref. [24]). This is in line with mechanical studies at MSH suggesting that the strength of lavas increased during the 2004–2008 eruption, becoming more crystalline and less porous, so that shear zones could localize[42], fault gauges develop and spines evolve[43]. This is further supported by our analog models, where we can directly observe spine formation as a result of frictional faulting originating from the conduit walls. Striations and slickensides on an exposed face of a spine demonstrate contact of the magma plug with the conduit wall[44]. Such structures are well described at MSH[2,45] or at the Unzen spine[46], commonly developing asymmetrically at the side exposed and depicting the whaleback. This structure is well reproduced by our models, which reveal a main shear zone on the side of the buttress and topographic high.

Observed fractures are consistent with extension as a result of bending of the spine, suggesting less brittle (or even partially viscous) behavior of the inner spine material. The fractures are located at the upper parts of the spine and are mostly oriented parallel to the collapse scar. We note that material heterogeneities of the Shiveluch spine are speculative, highlighting the need for more rigorous mechanical testing in the future. Different material strengths can result from compositional or textural variations, for example as a result from gas pressure or alteration-induced porosity changes[47]. While we recognize in our models that topography alone can explain an inclined extrusion direction of a dome and/or a spine, we find a similar or contributing effect results from heterogeneous material within the conduit. One may hypothesize that such material heterogeneity could be explained by differential degassing rates throughout the dome. Commonly, the conduit margins are highly permeable[1], so the magma at the margins can degas more effectively compared to magma located towards the center of the conduit. Additionally, heterogeneity may arise from previous eruptive history. For instance, we find that the spine is located to the S and SSW of previous eruptions and craters as described earlier[33]. Therefore the N and NNE side of the conduit and extruding spine is at or close to the location of an earlier conduit, which may have shattered or thermally affected the surrounding rocks.

Spines grow and collapse quickly, potentially leading to the formation of dangerous pyroclastic density currents. It is for this reason that we need to know more about their growth, as well as ways to safely monitor their growth (using remote sensing techniques, for example). Analysis of the Shiveluch spine may help to understand past volcanic activity and directionality of growth and collapse elsewhere. The collapse of the spine at Mount Pelée in mid-1903 produced a lethal pyroclastic density current[34]. With the new understanding of the relevance of previous topography and growth style, future spine extrusions may be more closely monitored with necessary actions being implemented to assess their hazard. It is important to precisely and safely measures the topography prior to spine formation, for which similar remote sensing techniques shown in this study may be used. For most of the 200 dome-building volcanoes worldwide, this information is still lacking and not regularly updated.

Methods

Time-lapse camera analysis. A camera was set up in Klyuchi town at 56.31888° 160.85687° at a distance of 43 km from the Shiveluch dome. The camera is a 3-megapixel Internet Stardot Netcam XL, taking images at 1024 × 768 px resolution every 1 min. Due to the large distance of the camera, the horizontal field of view is 7 km, translating to a 1 px dimension of 6.8 m. In other words, a spine growing to 100 m would be visible in only ~15 px. Most of the images are not usable due to poor visibility. Despite this and the low resolution, we find the information extracted for the growth rate is important. We first align the images using a digital image correlation approach[48]. The image stack was then preprocessed by brightness adjustment, normalizing the brightness of each image relative to the first image. This way, illumination changes are significantly reduced. Third, we apply a manual pixel tracking method, by picking and tracing the highest peak identified as the lava spine. Lastly, we converted all pixel units to meter scale, by picking locations of known distance in the field of view. Results show changes in elevation of the lava spine from March to September 2020. To account for possible measurement uncertainties, we repeated the tracking four times at different starting points, yielding a maximum vertical rise of 170.8, 167.5, 172.5, and 172.5 m, respectively, with a mean of 170.8 m and a standard deviation of 2.35 m. Uncertainties may be even higher, however, as these measurement errors do not take data errors resulting from camera shaking, optical deficiencies, and other artifacts into account.

Satellite radar observations. We used the synthetic aperture radar (SAR) data acquired every 11 days by the German radar satellite TerraSAR-X. The satellite is able to acquire data in high-resolution spotlight mode, which provides us with an acquisition type yielding a spatial resolution close to 1 m per pixel (px), which is about one order of magnitude better than most other radar data available. For Shiveluch we found a major advantage of the SAR technique was that it is an active sensor, thus the ground is illuminated by the sensor independent of day or night. The X-band wavelength passes through eruption clouds, and hence allows views of the cratered landscape, which is especially useful during a volcanic crisis[49]. We analyzed the acquisitions mainly in descending mode, with an 11-day repeat pass. Due to the complex topography and the side-looking radar line-of-sight, a geometric distortion may affect not only pixel locations but also the offsets of pixels. Accordingly, even symmetric deformations may appear asymmetrically. We note that ascending mode data also exists and was analyzed, but due to the large geometric distortion the growing spine is located in the foreshortening region (see Supplementary Fig. 3). An interferometric technique (InSAR) was not found to be valuable due to ash coverage, rapid reflectivity changes, and resulting decorrelation. Therefore, we exploited the amplitude information[38]; we stacked and coregistered the images using the GAMMA software. As the satellite sees the backscattered electromagnetic microwave radiation, each reflected pixel represents the proportion of power relative to the energy scattered and transmitted back. The X-band (wavelength of 31 mm and frequency of 9.6 GHz) amplitude depends on surface geometry, therefore the morphology and associated changes of the topography is expressed by amplitude images[50]. The measured amplitude accordingly depends on the sum of all scatterers within a ground resolution pixel. To avoid geocoding warping artifacts in the steep summit region, we analyzed the amplitude in radar coordinates. We used a particle image velocimetry (PIV) approach[24,48] to quantify offsets of groups of pixels in this amplitude image dataset.

Stereophotos and digital terrain modeling. We acquired and analyzed high-resolution optical images taken from a helicopter on October 22, 2019 (before the spine growth) and by the Pléiades satellite PHR1B sensor on October 01 and 13, 2020 (during the spine growth). The acquisition and photogrammetric processing of the 2019 aerial images is described in detail in ref. [33]. The tri-stereo Pleiades images were made during a single satellite pass, so that panchromatic 1 m resolution imagery could be used to develop orthophotos and DTMs. The data acquisition timing is mainly dependent on concurrent satellite passes and a (rare) clear sky condition. Processing of the data was realized in Erdas Imagine 2015 v15.1[9], where we used between 30 and 50 tie points for the relative orientation. A conversion from pixel scale to metric scale was employed using the Rational Polynomial Coefficients block adjustment approach. After the image orientation, we obtained photogrammetric models with a total root-mean-square error (RMSE) of 0.2 m. By using the Enhanced Automatic Terrain Extraction module (eATE) with normalized cross-correlation algorithm as implemented in the Erdas Imagine software, we were able to extract 2 m resolution point clouds referenced to the WGS84 coordinate system UTM57 zone. These point clouds were filtered with the CloudCompare v2.9.1 noise filter and then manually cleaned with the CloudCompare segmentation tool. The derived orthophotos and DEMs were used in the geoinformatics framework (ArcGIS 10.2.1) for analyzing shapes, azimuths, striations, and fractures. We manually traced all features and calculated the azimuthal direction for each lineament, necessary for rose diagram representations. We further computed the density of lineaments searching for the number of lines in a 70 m radius area, yielding up to 70 lineaments/area. The two orthophotos on October 01 and 12, 2020 were further used for manual tracking of relevant features and pixels, allowing us to derive the displacement in the field of view.

Modeling. We performed two complementary modeling strategies. Analog modeling was performed by extruding mixtures of sand and plaster powder onto a custom-built table. Experiments were recorded at a 30 s interval with a single camera facing horizontally onto a Plexiglas plate, enabling the observation of the dome and spine extrusion in a profile view. In separate tests, we found that boundary effects between the extruded sand and the plexiglas plate are apparent but negligible. The extrusion speed was set to 1.75 mm/min, although in the absence of viscous material the extrusion rate does not affect the extrusion and allows for a mainly geometric scaling[24]. To test the effect of heterogeneous material within the conduit, the experiments were modified to extrude cohesive and strong material from the conduit, corresponding to dense, degassed and brittle magma. Here, the sand mixture contained 30% plaster for the cohesive conduit[24]. In order to better reflect the local topography around the Shiveluch spine, one side was additionally buttressed by placing a barrier next to the conduit wall, thus preventing equal deposition on each side of the dome. To evaluate the experimental results, we employed Particle-Image-Velocimetry (PIV) on sequential images using the LaVision DaVis software package (version 10.0.5). Motions in the image field were extracted using multiple passes by applying a decreasing window size of 64 × 64 px at 50% overlap and 24 × 24 px at 75% overlap. This enabled the visualization of displacement vectors, particle strain, and vorticity to understand movement and structures during the dome and spine growth.

Numerical modeling was performed using commercially available software Particle Flow Code (PFC) from Itasca Consulting Group Ltd., and the method primarily follows that described earlier by[51,52], without distinct material behavior for a fluid core and a solid talus (because observations suggest spine material is so competent that it exhibits solid-like behavior). A two-dimensional discrete element method (DEM) is used[53] in this software. We consider heterogeneous conduit material with a cohesion on the left of 4 MPa and on the right of 1 MPa. Incorporation of cohesive strengths for the magma allows for simulation of non-Newtonian magmatic behavior[54,55]. The lower cohesion value is in line with estimates of bulk material cohesion for endogenous domes[56], whilst the higher cohesion value is artificially increased in line with estimates that spines require much more cohesive material in order to maintain observed heights[57]. To construct the numerical model geometry, a topographic profile from 2019 is used, with an additional buttress next to the conduit wall. The boundary conditions in the model are frictionally-controlled at the interaction between the dome material and the topography, meaning that this material resists rolling along the topography. Conduit dynamics (e.g., frictional slip at conduit margins) are not simulated here. Results from the DEM modeling are visualized in two ways: (1) by velocity vectors, similar to the PIV approach used for the analog models; and (2) the computation of normalized finite shear strain. The finite shear strain is computed by inverse strain modeling[58,59] and calculates the Cauchy–Green deformation tensor to compute maximum shear strain. This method highlights areas where groups of particles move as a coherent block relative to their neighbors, such that it picks out planes of failure or shear bands.

Data availability

The photogrammetric data by Pleiades are available via Kamchatka-Kuriles Supersite within Geohazard Supersites and Natural Laboratories Initiative (https://geo-gsnl.org/supersites). The photogrammetric data is available through the supplementary file or through a data publication with the https://doi.org/10.5281/zenodo.6420254 (weblink https://zenodo.org/record/6420254). Furthermore, the time-lapse webcam data can be accessed via https://doi.org/10.5281/zenodo.6420312 (weblink https://zenodo.org/record/6420312). Any other requests should be made to the first author. TerraSAR-X data available through the DLR eoweb service. Field photographs by Yury Demyanchuk available through the Kamchatka volcano observatory website http://volkstat.ru/index.php/2020/09/30/raboti-na-shv-i-krest/.

Received: 28 January 2022; Accepted: 30 June 2022;
Published online: 27 July 2022

References

1. Gaunt, H. E., Sammonds, P. R., Meredith, P. G., Smith, R. & Pallister, J. S. Pathways for degassing during the lava dome eruption of Mount St. Helens 2004–2008. *Geology* **42**, 947–950 (2014).
2. Kendrick, J. E. et al. Volcanic drumbeat seismicity caused by stick-slip motion and magmatic frictional melting. *Nat. Geosci.* **7**, 438–442 (2014).
3. Heap, M. J. et al. Hydrothermal alteration of andesitic lava domes can lead to explosive volcanic behaviour. *Nat. Commun.* https://doi.org/10.1038/S41467-019-13102-8i (2019).
4. Tanguy, J. C. Rapid dome growth at Montagne Pelee during the early stages of the 1902–1905 eruption: A reconstruction from Lacroix's data. *Bull. Volcanol.* **66**, 615–621 (2004).

5. Iverson, R. M. Dynamics of seismogenic volcanic extrusion resisted by a solid surface plug, Mount St. Helens 2004–2005. *US Geological Survey Professional Paper, Report* https://doi.org/10.3133/pp175021i (2008).
6. Watts, R. B., Herd, R. A., Sparks, R. S. J. & Young, S. R. Growth patterns and emplacement of the andesitic lava dome at Soufrière Hills, Montserrat. *Geol. Soc. London Memoir* **21**, 115–152 (2002).
7. Nakada, S. & Motomura, Y. Petrology of the 1991–1995 eruption at Unzen: Effusion pulsation and groundmass crystallization. *J. Volcanol. Geotherm. Res.* **89**, 173–196 (1999).
8. Kirsanov, I. & Studenikin, B. Y. Dynamics of Bezymianny volcano extrude eruption in 1965–1968. *Bull. Volcanol. Stat* **47**, 15–22 (1971).
9. Shevchenko, A. V. et al. The rebirth and evolution of Bezymianny volcano, Kamchatka after the 1956 sector collapse. *Nat. Commun. Earth Environ.* **1**, 15 (2020).
10. Calder, E. S., Lavallée, Y., Kendrick, J. E. & Bernstein, M. *The Encyclopedia of Volcanoes (Second Edition)* (ed Sigurdsson, H.) 343–362 (Academic Press, 2015).
11. Voight, B. Structural stability of andesite volcanoes and lava domes. *Phil. Trans. R. Soc. London* **358**, 1663–1703 (2000).
12. Heap, M. J., Russell, J. K. & Kennedy, L. A. Mechanical behaviour of dacite from Mount St. Helens (USA): A link between porosity and lava dome extrusion mechanism (dome or spine)? *J. Volcanol. Geotherm. Res.* **328**, 159–177 (2016).
13. Couch, S., Sparks, R. S. J. & Carroll, M. R. The kinetics of degassing-induced crystallization at Soufrière Hills Volcano, Montserrat. *J. Petrol.* **44**, 1477–1502 (2003).
14. Druitt, T. H. et al. Episodes of cyclic Vulcanian explosive activity with fountain collapse at Soufriere Hills Volcano, Montserrat. *Memoirs Geol. Soc. London* **21**, 281–306 (2002).
15. Cashman, K. V., Thornber, C. R. & Pallister, J. S. From dome to dust: Shallow crystallization and fragmentation of conduit magma during the 2004–2006 dome extrusion of Mount St. Helens, Washington. Report No. 1750-19, 387–413 https://doi.org/10.3133/pp175019 (Reston, VA, 2008).
16. Vallance, J. W., Schneider, D. J. & Schilling, S. P. Growth of the 2004–2006 lava-dome complex at Mount St. Helens, Washington. *USGS Professional Paper* https://doi.org/10.3133/pp17509i (2008).
17. Anderson, K. & Segall, P. Physics-based models of ground deformation and extrusion rate at effusively erupting volcanoes. *J. Geophys. Res.: Solid Earth* https://doi.org/10.1029/2010JB007939i (2011).
18. Pallister, J. S. et al. Petrology of the 2004–2006 Mount St. Helens lava dome–implications for magmatic plumbing and eruption triggering. *USGS Professional Paper* https://doi.org/10.3133/pp175030i (2008).
19. Salzer, J. T. et al. Volcano dome dynamics at Mount St. Helens: Deformation and intermittent subsidence monitored by seismicity and camera imagery pixel offsets. *J. Geophys. Res.: Solid Earth* **121**, 7882–7902 (2016).
20. Jiao, L. et al. Necking and fracking may explain stationary seismicity and full degassing in volcanic silicic spine extrusion. *Earth Planet. Sci. Lett.* **503**, 47–57 (2018).
21. Melnik, O. & Sparks, S. *The Eruption of Soufriere Hills Volcano, Montserrat* Vol. 21 (eds Druitt, T. H. & Kokelaar, B. P.) 153–171 (Geological Society London, Memoirs, 2002).
22. Kennedy, L. A. & Russell, J. K. Cataclastic production of volcanic ash at Mount Saint Helens. *Phys. Chem. Earth, Parts A/B/C* **45–46**, 40–49 (2012).
23. Dzurisin, D., Lisowski, M., Poland, M. P., Sherrod, D. R. & LaHusen, R. G. Constraints and conundrums resulting from ground-deformation measurements made during the 2004–2005 dome-building eruption of Mount St. Helens, Washington. *USGS Professional Paper* https://doi.org/10.3133/pp175014i (2008).
24. Zorn, E. U., Walter, T. R., Heap, M. J. & Kueppers, U. Insights into lava dome and spine extrusion using analogue sandbox experiments. *Earth Planet. Sci. Lett.* https://doi.org/10.1016/J.Epsl.2020.116571i (2020).
25. Ryan, A. G., Heap, M. J., Russell, J. K., Kennedy, L. A. & Clynne, M. A. Cyclic shear zone cataclasis and sintering during lava dome extrusion: Insights from Chaos Crags, Lassen Volcanic Center (USA). *J. Volcanol. Geotherm. Res.* **401**, 106935 (2020).
26. Gorbach, N. V., Portnyagin, M. V. & Philosofova, T. M. Dynamics of exrtrusive dome growth and variations in chemical and mineralogical composition of Young Shiveluch andesites in 2001–2013. *J. Volcanol. Seismol.* **10**, 360–381 (2016).
27. Gorelchik, V. I., Shirokov, V. A., Firstov, P. P. & Chubarova, O. S. Shiveluch volcano: Seismicity, deep structure and forecasting eruptions (Kamchatka). *J. Volcanol. Geotherm. Res.* **78**, 121–137 (1997).
28. Pevzner, M. M., Tolstykh, M. L. & Babansky, A. D. The Shiveluch Volcanic Massif, Kamchatka: Stages in the evolution of a magmatic system: Results of geochronological and thermobarogeochemical studies. *J. Vol. Seismol.* **12**, 242–251 (2018).
29. Belousov, A., Belousova, M. & Voight, B. Multiple edifice failures, debris avalanches and associated eruptions in the Holocene history of Shiveluch volcano, Kamchatka, Russia. *Bull. Volcanol.* **61**, 324–342 (1999).
30. Gorshkov, G. & Dubik, Y. M. Gigantic directed blast at Shiveluch volcano (Kamchatka). *Bull. Volcanol.* **34**, 261–288 (1970).
31. Belousov, A. B. The Shiveluch volcanic eruption of 12 November 1964—explosive eruption provoked by failure of the edifice. *J. Volcanol. Geotherm. Res.* **66**, 357–365 (1995).
32. Koulakov, I. et al. Mantle and crustal sources of magmatic activity of Klyuchevskoy and surrounding volcanoes in Kamchatka inferred from earthquake tomography. *J. Geophys. Res.: Solid Earth* **125**, e2020JB020097 (2020).
33. Shevchenko, A. V. et al. Constructive and destructive processes during the 2018–2019 Eruption Episode at Shiveluch Volcano, Kamchatka, studied from satellite and aerial data. *Front Earth Sc-Switz* https://doi.org/10.3389/Feart.2021.680051i (2021).
34. Lacroix, A. F. A. *La montagne Pelée et ses éruptions* (Masson, pour l'Académie des Sciences, 1904).
35. Burgisser, A. & Degruyter, W. *The Encyclopedia of Volcanoes (Second Edition)* (ed Sigurdsson, H.) 225–236 (Academic Press, 2015).
36. Belousov, A., Belousova, M., Auer, A., Walter, T. R. & Kotenko, T. Mechanism of the historical and the ongoing Vulcanian eruptions of Ebeko volcano, Northern Kuriles. *Bull. Volcanol.* https://doi.org/10.1007/s00445-020-01426-zi (2021).
37. Huppert, H. E., Shepherd, J. B., Haraldur Sigurdsson, R. & Sparks, S. J. On lava dome growth, with application to the 1979 lava extrusion of the soufrière of St. Vincent. *J. Volcanol. Geotherm. Res.* **14**, 199–222 (1982).
38. Walter, T. R. et al. Imaging the 2013 explosive crater excavation and new dome formation at Volcan de Colima with TerraSAR-X, time-lapse cameras and modelling. *J. Volcanol. Geotherm. Res.* **369**, 224–237 (2019).
39. Hale, A. J. & Wadge, G. The transition from endogenous to exogenous growth of lava domes with the development of shear bands. *J. Volcanol. Geotherm. Res.* **171**, 237–257 (2008).
40. Scott, W. E., Sherrod, D. R. & Gardner, C. A. Overview of the 2004 to 2006, and continuing, eruption of Mount St. Helens, Washington. Report No. 1750-1, 3-22 https://doi.org/10.3133/pp17501 (Reston, VA, 2008).
41. Moran, S. C. et al. Seismicity associated with renewed dome building at Mount St. Helens, 2004–2005. *US Geological Survey professional paper*, 27–60 https://doi.org/10.3133/pp17502 (2008).
42. Smith, R., Sammonds, P. R., Tuffen, H. & Meredith, P. G. Evolution of the mechanics of the 2004–2008 Mt. St. Helens lava dome with time and temperature. *Earth Planet. Sci. Lett.* **307**, 191–200 (2011).
43. Ryan, A. G., Friedlander, E. A., Russell, J. K., Heap, M. J. & Kennedy, L. A. Hot pressing in conduit faults during lava dome extrusion: Insights from Mount St. Helens 2004–2008. *Earth Planet. Sci. Lett.* **482**, 171–180 (2018).
44. Kendrick, J. E. et al. Extreme frictional processes in the volcanic conduit of Mount St. Helens (USA) during the 2004–2008 eruption. *J. Struct. Geol.* **38**, 61–76 (2012).
45. Iverson, R. M. et al. Dynamics of seismogenic volcanic extrusion at Mount St Helens in 2004–05. *Nature* **444**, 439–443 (2006).
46. Lamb, O. D. et al. Repetitive fracturing during spine extrusion at Unzen volcano, Japan. *Solid Earth* **6**, 1277–1293 (2015).
47. Heap, M. J. et al. Hydrothermal alteration can result in pore pressurization and volcano instability. *Geology* https://doi.org/10.1130/g49063.1i (2021).
48. Walter, T. R. Low cost volcano deformation monitoring: optical strain measurement and application to Mount St. Helens data. *Geophys. J. Int.* **186**, 699–705 (2011).
49. Pallister, J. S. et al. Merapi 2010 eruption-chronology and extrusion rates monitored with satellite radar and used in eruption forecasting. *J. Volcanol. Geotherm. Res.* **261**, 144–152 (2013).
50. Wadge, G. et al. Rapid topographic change measured by high-resolution satellite radar at Soufriere Hills Volcano, Montserrat, 2008–2010. *J. Volcanol. Geotherm. Res.* **199**, 142–152 (2011).
51. Harnett, C. E., Thomas, M. E., Purvance, M. D. & Neuberg, J. Using a discrete element approach to model lava dome emplacement and collapse. *J. Volcanol. Geotherm. Res.* **359**, 68–77 (2018).
52. Harnett, C. E. & Heap, M. J. Mechanical and topographic factors influencing lava dome growth and collapse. *J. Volcanol. Geotherm. Res.* **420**, 107398 (2021).
53. Cundall, P. A. & Strack, O. D. L. A discrete numerical model for granular assemblies. *Géotechnique* **29**, 47–65 (1979).
54. Blake, S. *Lava Flows and Domes: Emplacement Mechanisms and Hazard Implications* (ed Fink, J. N.) 88–126 (Springer, 1990).
55. Lavallée, Y., Hess, K.-U., Cordonnier, B. & Bruce Dingwell, D. Non-Newtonian rheological law for highly crystalline dome lavas. *Geology* **35**, 843–846 (2007).
56. Simmons, J., Elsworth, D. & Voight, B. Instability of exogenous lava lobes during intense rainfall. *Bull. Volcanol.* **66**, 725–734 (2004).
57. Husain, T., Elsworth, D., Voight, B., Mattioli, G. & Jansma, P. Influence of extrusion rate and magma rheology on the growth of lava domes: Insights from particle-dynamics modeling. *J. Volcanol. Geotherm. Res.* **285**, 100–117 (2014).
58. Morgan, J. K. & McGovern, P. J. Discrete element simulations of gravitational volcanic deformation: 1. Deformation structures and geometries. *J. Geophys. Res.: Solid Earth* https://doi.org/10.1029/2004JB003252i (2005).

59. Schöpfer, M. P. J., Childs, C. & Walsh, J. J. Two-dimensional distinct element modeling of the structure and growth of normal faults in multilayer sequences: 1. Model calibration, boundary conditions, and selected results. *J. Geophys. Res.: Solid Earth* https://doi.org/10.1029/2006JB004902i (2007).
60. Jenness, J. *Polar plots for ArcGIS* (Jenness Enterprises, 2014).

Acknowledgements

TerraSAR-X data provided through a DLR_TSX agreement (GEO1505). The authors thank the Geohazard Supersites and Natural Laboratories Initiative (https://geo-gsnl.org/supersites) for providing Pleiades satellite data, and the Planet Team, 2017 for providing the Planet data via the Planet application program interface (https://api.planet.com). CH acknowledges support from the Royal Irish Academy Charlemont Grant call. The content of this publication is solely the responsibility of the authors and does not necessarily represent the official views of the Royal Irish Academy.

Author contributions

T.R.W. analyzed optical, TerraSAR-X, and Pleiades data and lead the writing of the manuscript, E.Z. realized sandbox models and analysis, C.H. realized numerical models and analysis, A.B. and M.B. have monitored the growth of the spine using webcams and field observations, A.V.S. has processed the aerial and Pleiades data, M.V. contributed to satellite imagery.

Funding

Open Access funding enabled and organized by Projekt DEAL.

Competing interests

The authors declare no competing interests.

Additional information

Supplementary information The online version contains supplementary material available at https://doi.org/10.1038/s43247-022-00491-w.

Correspondence and requests for materials should be addressed to Thomas R. Walter.

Peer review information *Communications Earth & Environment* thanks Paul Lundgren and the other, anonymous, reviewer(s) for their contribution to the peer review of this work. Primary Handling Editors: Teng Wang and Joe Aslin.

Reprints and permission information is available at http://www.nature.com/reprints

Publisher's note Springer Nature remains neutral with regard to jurisdictional claims in published maps and institutional affiliations.

Open Access This article is licensed under a Creative Commons Attribution 4.0 International License, which permits use, sharing, adaptation, distribution and reproduction in any medium or format, as long as you give appropriate credit to the original author(s) and the source, provide a link to the Creative Commons license, and indicate if changes were made. The images or other third party material in this article are included in the article's Creative Commons license, unless indicated otherwise in a credit line to the material. If material is not included in the article's Creative Commons license and your intended use is not permitted by statutory regulation or exceeds the permitted use, you will need to obtain permission directly from the copyright holder. To view a copy of this license, visit http://creativecommons.org/licenses/by/4.0/.

© The Author(s) 2022